Lawrence Berkeley National Laboratory
LBL Publications

Title
Optoelectronic and spectroscopic characterization of vapour-transport grown Cu 2 ZnSnS 4 single crystals

Permalink
https://escholarship.org/uc/item/5nt8d2pd

Journal
Journal of Materials Chemistry A, 5(3)

ISSN
2050-7488

Authors
Ng, Tat Ming
Weller, Mark T
Kissling, Gabriela P
et al.

Publication Date
2017

DOI
10.1039/c6ta09817g

Peer reviewed

eScholarship.org Powered by the California Digital Library
University of California

Journal of Materials Chemistry A

PAPER

View Article Online
View Journal

Published on 12 December 2016. Downloaded by University of Milan - Bicocca on 09/01/2017 13:31:27.

Cite this: DOI: 10.1039/c6ta09817g

Optoelectronic and spectroscopic characterization of vapour-transport grown Cu_2ZnSnS_4 single crystals†

Tat Ming Ng,[ab] Mark T. Weller,[b] Gabriela P. Kissling,‡[b] Laurence M. Peter,*[b] Phillip Dale,[c] Finn Babbe,[c] Jessica de Wild,[c] Bernard Wenger,[d] Henry J. Snaith[d] and David Lane[e]

Single crystals of Cu_2ZnSnS_4 (CZTS) have been grown by iodine vapor transport with and without addition of NaI. Crystals with tin-rich copper-poor and with zinc-rich copper-poor stoichiometries were obtained. The crystals were characterized by single crystal X-ray diffraction, energy-dispersive X-ray spectroscopy, photocurrent spectroscopy and electroreflectance spectroscopy using electrolyte contacts as well as by spectroscopic ellipsometry, Raman spectroscopy and photoluminescence spectroscopy (PL)/decay. Near-resonance Raman spectra indicate that the CZTS crystals adopt the kesterite structure with near-equilibrium residual disorder. The corrected external quantum efficiency of the p-type crystals measured by photocurrent spectroscopy approaches 100% close to the bandgap energy, indicating efficient carrier collection. The bandgap of the CZTS crystals estimated from the external quantum efficiency spectrum measured using an electrolyte contact was found to be 1.64–1.68 eV. An additional sub-bandgap photocurrent response (Urbach tail) was attributed to sub bandgap defect states. The room temperature PL of the crystals was attributed to radiative recombination *via* tail states, with lifetimes in the nanosecond range. At high excitation intensities, the PL spectrum also showed evidence of direct band to band transitions at ~1.6 eV with a shorter decay time. Electrolyte electroreflectance spectra and spectra of the third derivative of the optical dielectric constant in the bandgap region were fitted to two optical transitions at 1.71 and 1.81 eV suggesting a larger valence band splitting than predicted theoretically. The high values of the EER broadening parameters (192 meV) indicate residual disorder consistent with the existence of tail states.

Received 13th November 2016
Accepted 12th December 2016

DOI: 10.1039/c6ta09817g

www.rsc.org/MaterialsA

Introduction

The kesterites Cu_2ZnSnS_4 (CZTS) and $Cu_2ZnSnSe_4$ (CZTSe) continue to excite interest as potential earth-abundant alternatives to $CuIn_xGa_{(1-x)}Se_2$ (CIGSe) for application as absorber materials in thin film solar cells.[2–6] By 2014, the efficiency of kesterite solar cells had reached 12.6%,[7] but progress since then has focused mainly on developing safer non-toxic routes to fabrication of CZTS(Se) absorber layers. The main limiting factor for device performance is the open circuit voltage, which is ~200 mV lower than that of CIGSe cells with comparable bandgaps. The reasons for the voltage losses in kesterite cells are still not clear.[6] One possible cause is enhanced recombination due to tail states arising from Cu/Zn disorder,[8,9] but a recent review of the evidence for this explanation failed to reach a firm conclusion.[10] Alternative explanations include enhanced surface recombination at grain boundaries[11] and the influence of secondary phases.[6] In order to discover more about the bulk properties of CZTS, we have grown single crystals with different stoichiometric compositions by iodine vapor transport[12] (with and without the addition of NaI as a sodium source) and have characterized their optoelectronic properties using photocurrent spectroscopy with electrolyte contacts (PS) as well as electrolyte electroreflectance spectroscopy (EER), spectroscopic ellipsometry (SE), Raman spectroscopy and photoluminescence (PL).

[a]Centre for Sustainable Chemical Technologies, University of Bath, Bath BA2 7AY, UK
[b]Department of Chemistry, University of Bath, Bath BA2 7AY, UK. E-mail: l.m.peter@bath.ac.uk
[c]Physics and Materials Science Research Unit, University of Luxembourg, 41, rue du Brill, L-4422 Belvaux, Luxembourg
[d]University of Oxford, Clarendon Laboratory, Parks Road, Oxford, OX13PU, UK
[e]Cranfield Forensic Institute, Cranfield University, Defence Academy of the United Kingdom, Shrivenham, SN6 8LA, UK

† Electronic supplementary information (ESI) available: Oven cooling curve. Raman spectra/fitting. Comparison of SE data with ref. 1 Vineyard model and calculations. PL spectra/decay for needle. Tauc and Urbach plots. Gärtner analysis. Impedance data. EER results and validation of low field approximation. See DOI: 10.1039/c6ta09817g

‡ Present address: Department of Chemistry, University of Southampton, Southampton SO17 1BJ, UK.

Published on 12 December 2016. Downloaded by University of Milan - Bicocca on 09/01/2017 13:31:27.

It is possible to grow single phase kesterite materials with significant deviations from stoichiometry.[13] In this work, we have focused on zinc-rich/copper poor and tin-rich/copper poor materials because copper-poor stoichiometries give the best efficiencies in solar cells.[14] Our primary objectives included determination of the stoichiometry and bandgap of the single crystals and assessment of the optical properties. In addition, we have examined the dependence of the degree of substitutional disorder on composition and annealing conditions.

Analysis of the single crystal X-ray diffraction data from the Cu_2ZnSnS_4 crystals is unable to demonstrate unequivocally that they have the kesterite structure. Dumcenco *et al.*[15] have used Raman scattering to establish that CZTS crystals grown by chemical vapor transport adopt the kesterite phase. For our crystals, the presence of the kesterite phase is supported by the peak assignments in the near-resonance Raman spectra, which also showed that the as-grown crystals have a low level of disorder comparable with that achieved by low temperature (150 °C) annealing of fully disordered crystals for 24 hours.

The results obtained by PS for etched single crystals indicate that carrier collection is highly efficient in the voltage-biased single crystal/electrolyte junction, with external quantum efficiencies (EQE) corrected for reflection approaching 100%. The experimental EQE spectrum was compared with spectra calculated for different carrier collection depths using the absorption coefficient data obtained by spectroscopic ellipsometry (SE). The onset seen in the photocurrent excitation spectrum is much sharper than in the absorption spectrum derived from SE, allowing more reliable determination of the bandgap from Tauc plots. The bandgap values obtained by the Tauc/EQE analysis (1.64–1.68 eV) are close to the 1.64 eV reported by Fernandes *et al.*[16] for CZTS layers prepared from sulfurized metallic precursors, although they are considerably higher than values reported, for example, by Li *et al.*[1] for polycrystalline thin films prepared by reactive sputtering (1.55–1.59 eV). Line shape fitting of the EER spectra and the third derivative of the optical dielectric constant obtained by SE reveals two optical transitions at 1.71 eV and 1.81 eV with substantial spectral broadening (Γ = 192 meV) attributed to the presence of residual disorder, even in as-grown slow-cooled samples with near equilibrium disorder. The observed separation between the two transitions (100 meV) is larger than the crystal field splitting calculated for kesterite CZTS (40 meV) by Persson *et al.*[17]

Experimental details

The synthesis of CZTS single crystals using iodine vapor transport in a two zone furnace has been described elsewhere.[12] The CZTS starting materials were synthesized in evacuated sealed quartz ampules using the metals (Cu 99.7%, Zn 99.9%, Sn 99.85%) and elementary sulfur (99.999%). Vapor transport growth was carried out using 99.999% iodine. The effect of adding sodium was investigated in one of the growth runs by adding 1% (w/w) sodium iodide (99+%) to the CZTS starting material. The crystals were cooled naturally to room temperature over 24 hours after the oven was switched off. Further details, including the stoichiometric composition of the synthesis mixtures as well as the oven cooling curve are given in the ESI.† The as-grown crystals were rinsed in chloroform and isopropanol to remove traces of iodine.

Single-crystal X-ray diffraction (SXD) data were collected at room temperature operating with Mo-K_α radiation (λ = 0.71073 Å) (Agilent Xcalibur). Structures were solved using the WinGX suite of programmes,[18] utilizing XPREP[19] and SHELX-97,[20] by direct methods.[21] For the two crystal types obtained (needles and platelets), analysis was undertaken using the models reported in the literature for kesterite (in space group $I\bar{4}$) and stannite (space group $I\bar{4}2m$) descriptions of Cu_2ZnSnS_4.[22]

Elemental analysis of the materials was carried out using energy-dispersive X-ray spectroscopy (EDS) (10 and 20 kV, Oxford Instruments).

Near-resonance Raman measurements were performed at room temperature under ambient atmosphere (Renishaw inVia). A linearly polarized laser beam (785 nm) was focused into a spot size ~5 μm in diameter. Prior to the measurements, the system was calibrated with polycrystalline Si at 520 cm^{-1}.

The crystals were etched in saturated Na_2S solution followed by 30% H_2O_2/1 M H_2SO_4. After rinsing, the samples were treated with 1 M HCl, to remove metal (hydr)oxides. Crystals treated in this way are referred to in the text as 'etched'.

Further details of the PC, PL, EER, SE and Raman measurements and fitting procedures are given in the ESI†. For the PC and EER measurements, the mounted and etched kesterite crystals were contacted on the abraded rear side with an evaporated gold contact. Measurements were made using an air-saturated 0.1 M acetate buffer electrolyte (pH 4.5) in a 3-electrode cell with platinum counter and Ag|AgCl reference electrodes controlled by a battery-operated low-noise potentiostat.

Results and discussion

Composition and degree of disorder of the kesterite phase

Two main crystal shapes were obtained from the iodine vapor transport growth: needles (no sodium present in starting material) and platelets (1% w/w NaI present in starting material). Fig. 1 shows examples of the two types. Both crystals exhibited one smooth reflective surface suitable for SE and EER measurements.

The averaged elemental compositions of the crystals determined by EDS at 6 different points on each crystal are summarized in Table 1. The standard deviations are shown in brackets. The level of sodium (if present) in the platelet was below the limit of detection by EDS (the sensitivity is limited by

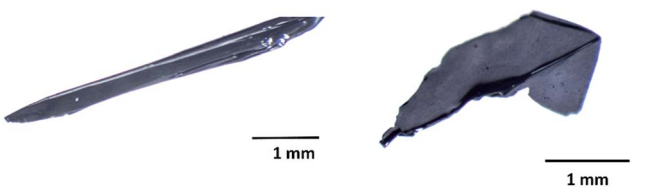

Fig. 1 Typical shapes of the Cu_2ZnSnS_4 crystals grown by iodine vapor transport. The platelet on the right was grown from CZTS starting material containing 1% (w/w) NaI.

 This journal is © The Royal Society of Chemistry 2016

Published on 12 December 2016. Downloaded by University of Milan - Bicocca on 09/01/2017 13:31:27.

Table 1 Elemental composition of Cu_2ZnSnS_4 crystals as determined by energy dispersive X-ray spectroscopy

Type	Cu	Zn	Sn	S	Cu/(Zn + Sn)
Needle	22.6 (±0.4)	14.2 (±0.9)	12.5 (±0.4)	50.7 (±0.4)	0.85 (±0.5)
Platelet	22.8 (±0.6)	12.1 (±0.6)	13.3 (±0.7)	51.9 (±1.0)	0.90 (±0.5)

the overlap of the Na and Zn peaks). The sodium concentration determined by atomic absorption spectroscopy corresponded to 0.13 mol% in the platelet sample. No iodine was detected in either crystal after rinsing in chloroform and isopropanol.

The compositions of the two types of crystal are illustrated in the pseudo ternary phase diagram shown in Fig. 2. The classification into type A, B, C, D and E follows the notation used by Choubrac *et al.*[23–25]

The needle composition is close to the A type line, which corresponds to the substitution

$$2Cu \rightarrow V_{Cu} + Zn_{Cu}$$

whereas the platelet stoichiometry is closer to the E type[26] line, which corresponds to the substitution

$$2Cu + Zn \rightarrow 2V_{Cu} + Sn_{Zn}$$

XRD structure analysis

Distinguishing between the kesterite and stannite structures of CZTS, which differ only in the ordering of the near isoelectronic copper and zinc atoms is not generally possible using laboratory X-ray data. Only anomalous-scattering X-ray single crystal diffraction[27] and neutron single crystal diffraction can fully distinguish the two copper and zinc distributions. Powder neutron diffraction has been proposed as a way of distinguishing the two structure descriptions,[28] but this approach is not reliable as a consequence of peak multiplicities in powder methods. In addition to the copper and zinc ordering, the sulfur position in the kesterite $I\bar{4}$ space group can be displaced on to a general (x, y, z) position (from x, x, z), potentially modifying reflection intensities.

For both needle and platelet crystals, the structure was solved and refined using the kesterite model in the space group $I\bar{4}$.

For the platelet, a final R_1 of 2.68% and wR_2 = 7.04% was obtained, and corresponding values for the needle were $R_1 = 2.13\%$ and w$R_2 = 6.24\%$. Refinements using the disordered stannite description showed marginally worse R-factors but not significant enough to completely discount the stannite structure. No evidence of lowering of the lattice type to primitive, as in the $P\bar{4}2c$ description of Cu/Zn ordered CZTS, was observed in the single crystal XRD data. The results are summarized in Table 2.

Small but significant differences in the unit cell volume were found for the two crystal types, with the platelets giving a 0.08% higher value than the needle.

In view of the problems with the XRD interpretation, identification of the crystal structure as that of the kesterite was based on the Raman analysis described in the next section.

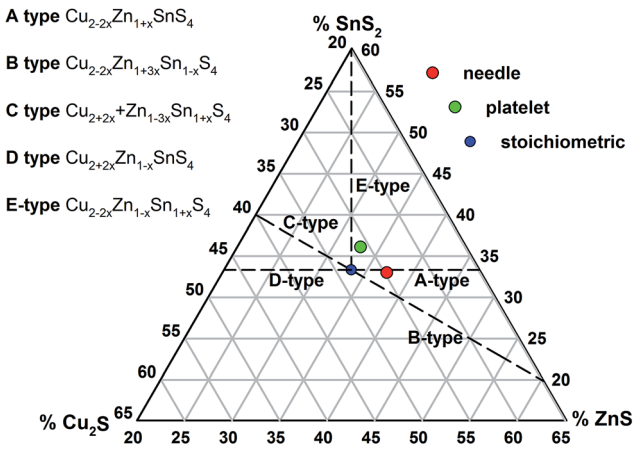

Fig. 2 Pseudo-ternary phase diagram for Cu_2ZnSnS_4 showing composition of the two sample types used in the study.

Raman spectroscopy: phase identification and disorder

Dumcenco *et al.*[15] used Raman spectroscopy to identify the kesterite crystal structure of CZTS single crystals grown by chemical vapor transport. These authors compared the observed Raman spectra with the results of theoretical calculations[29,30] for the kesterite and stannite crystal structures. A similar analysis for both types of our as-grown crystals confirms that they too have the kesterite structure (see the peak assignments and comparison with the results of the theoretical calculations given in the ESI†).

Disorder is a key issue in kesterites.[8,10,28,31,32] Studies of the order/disorder transition in CZTS[26,33,34] have shown that the degree of Cu/Zn antisite disorder exhibits second-order phase transition behaviour, with the complete disorder occurring at temperatures above *ca.* 280 °C. Paris *et al.*[35] have shown how

Table 2 Summary of single crystal XRD analysis

	Needle	Platelet
a/Å	5.4282(1)	5.4289(1)
c/Å	10.8198(5)	10.8256(5)
Unit cell volume/Å^3	318.809(19)	319.062(19)
Temperature/K	298	298
R indices observed data	$R_1 = 0.0213$	$R_1 = 0.0268$
	w$R_2 = 0.0624$	w$R_2 = 0.0704$
GooF	1.038	0.846

Published on 12 December 2016. Downloaded by University of Milan - Bicocca on 09/01/2017 13:31:27.

solid state NMR and Raman spectroscopy can be used to assess disorder in CZTS, and Rudisch *et al.*[33] have correlated Raman spectra with the degree of Cu/Zn disorder defined by the order parameter S, which is given by

$$S = \frac{P(\mathrm{Cu_{2c}}) - a_{2c}}{1 - a_{2c}} = 2P(\mathrm{Cu_{2c}}) - 1 = 2P(\mathrm{Zn_{2d}}) - 1 \qquad (1)$$

here $P(\mathrm{Cu_{2c}})$ and $P(\mathrm{Zn_{2d}})$ are the probabilities that Cu and Zn atoms occupy the 2c and 2d sites in the kesterite structure respectively, and a_{2c} (=0.5) is the fraction of 2c sites in the $z = 1/4$, 3/4 lattice planes as discussed by Scragg *et al.*[8]

Rey *et al.*[36] have discussed the dynamics of the order/disorder transition for $Cu_2ZnSnSe_4$ (CZTSe) using the Vineyard model,[37] which predicts the temperature and time dependence of S for vacancy and direct interchange mechanisms (see ESI†). Since we are dealing with a second order phase transformation, perfect ordering can only exist at 0 K. In practice, the highest achievable value of S is determined by the temperature dependence of the kinetics of atom interchange: at low temperatures (below *ca.* 150 °C), the disorder becomes 'frozen in' on a realistic time scale. The calculations based on the Vineyard model that are shown in the ESI† suggest that the highest values of S achievable by prolonged low temperature annealing will be in the range 0.7–0.8.

The degree of ordering of the as-grown crystals was assessed from near-resonance Raman spectra (excitation 785 nm). Fig. 3 contrasts the Raman spectrum of an as-grown platelet with the spectrum obtained after annealing at 300 °C and quenching to freeze in complete disorder. The fully disordered crystal was then annealed at 150 °C for 24 hours to induce equilibrium ordering (*cf.* Fig. 3). The Raman spectrum of this sample resembles that of the as-grown crystal, indicating that near-equilibrium ordering occurs during the slow cooling of the crystals in the furnace. Similar trends in S as a function of annealing temperature have been reported by Rudisch *et al.*[33] for polycrystalline CZTS films prepared by reactive sputtering.

Paris *et al.*[35] have suggested that a measure of the degree of Cu/Zn disorder is provided by the use of two empirical parameters, Q and Q', defined in terms of the intensity ratios of the main near-resonance Raman peaks as follows.

$$Q = I_{287}/I_{303},\ Q' = I_{338}/(I_{366} + I_{374}) \qquad (2)$$

Fig. 4 illustrates the deconvolution of the Raman spectra used to obtain the relative peak intensities for the case of the disordered platelet sample. The deconvolution of the Raman spectrum of the ordered platelet as well as the spectrum for the as-grown needle sample are given in the ESI.† Table 3 lists the Q and Q' values obtained using spectra measured on the platelet sample at two different spots and averaged before and after disordering.

For of the as-grown platelet, Q is higher than values reported for low temperature annealed CZTS films prepared by Scragg *et al.*[9] (stoichiometric CZTS, $Q < 2.5$) and by Rudisch *et al.*[33] (type B CZTS, $Q < 3.3$) using reactive sputtering. It is also higher than the value of 8.2 reported by Paris *et al.*[35] for slow-cooled (10 °C per h) – and hence relatively highly ordered – bulk polycrystalline type A CZTS. Similarly, Q' is higher than the value of 3.6 reported by the same authors for slow-cooled type A material.

We conclude that the as-grown platelet used in our study has ordering close to the equilibrium value for ~100–150 °C. The corresponding S value is unknown, but if the Vineyard model calculation in the ESI† is used as a guide, it would be in the range 0.7–0.8. Even if this level of ordering were achieved, it would still leave around 20–30% of the sites disordered, with significant consequences for band gap fluctuations and band gap tailing.

The Q and Q' values for the as-grown needle sample are both lower at around 5 and 3.5 respectively, suggesting that it may be less ordered than the platelet.

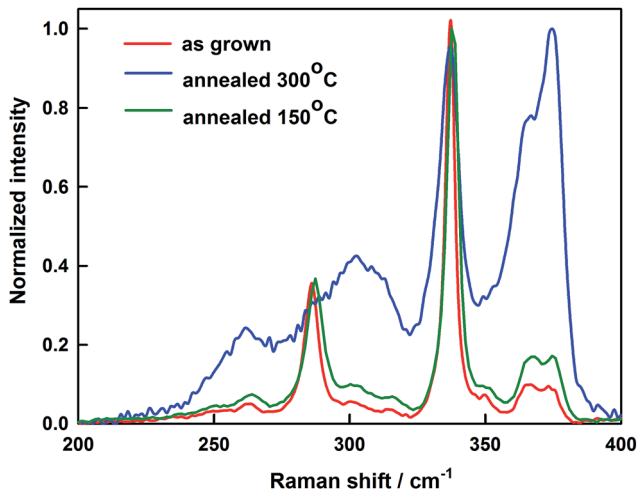

Fig. 3 Near-resonance Raman spectrum of as-grown CZTS platelet crystal compared with the spectrum of the fully disordered crystal (annealed at 300 °C). The spectrum obtained after annealing the disordered crystal for 24 h at 150 °C shows that near-equilibrium ordering is re-established.

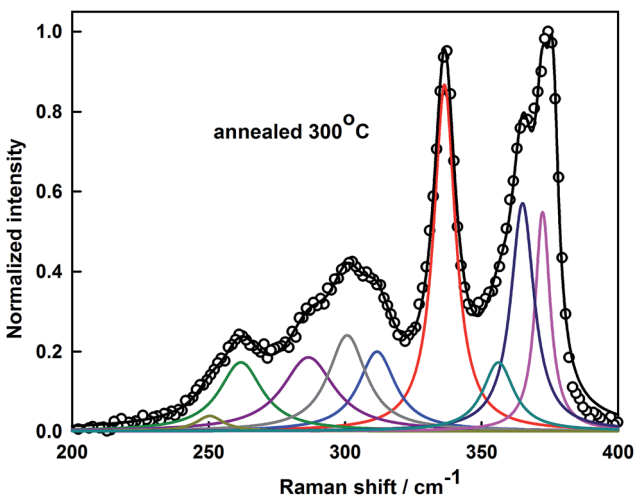

Fig. 4 Illustration of the fitting of the near-resonance Raman spectrum of the fully disordered CZTS platelet used to obtain the parameters Q and Q'.

This journal is © The Royal Society of Chemistry 2016

Published on 12 December 2016. Downloaded by University of Milan - Bicocca on 09/01/2017 13:31:27.

Table 3 Q and Q' values of copper-poor platelet sample as a function of annealing conditions

Annealing	Q	Q'
As-Grown	9.1 ± 1.1	5.7 ± 0.3
Annealed 300 °C	0.75 ± 0.40	0.8 ± 0.1

Photoluminescence

Fig. 5 shows the room temperature PL spectrum of the platelet crystal. The peak of the spectrum at 1.35 eV is substantially red shifted with respect to the bandgap of the material (1.68–1.71 eV – see below), which is consistent with emission taking place from tail states associated with disorder in the crystal. The intensity dependence of the peak position shown in the inset to Fig. 5 corresponds to a blue shift of 13 meV per decade, which agrees well with reported values.[38,39]

The PL spectrum for the needle exhibits a similar blue shift with a higher slope of 18 meV per decade (see ESI†). The blue shift seen for both CZTS crystals can be interpreted as an indication of potential fluctuations in the material.[40]

The dependence of the PL emission intensity on laser power for different samples (shown in the ESI†) corresponds to a power law PL $\propto I^m$, with m values ranging from 1.3–1.6. Levcenko *et al.* have reported a similar m value (1.3) for solution-processed CZTS layers. In the case of low temperature PL, m values greater than unity are usually attributed to band to band transitions,[41] but the value has more limited significance in the case of room temperature PL. Nevertheless, we conclude that the main PL peak is associated with near band edge (tail) states.

At higher intensities, a second peak becomes evident as a shoulder in the room temperature PL spectrum as illustrated by the semi-logarithmic plot in Fig. 6. Gershon *et al.*[42] have reported the emergence of a higher energy PL peak for high efficiency CZTS devices measured at 4 K, and have attributed it to free carrier recombination. These authors compared the PL lifetimes at 4 K for the low energy (1.16 eV) and high energy (1.43 eV) peaks. The low energy emission decayed on a time scale of microseconds (lifetime *ca.* 12 μs), indicating carrier trapping, whereas the high-energy component gave a much shorter lifetime of 1.7 ns, which is attributed to free carrier recombination not requiring activation by thermal excitation from tail states. Although there are problems in comparing low temperature measurements with our results, it seems reasonable to assume that the high-energy peak in the room temperature PL spectrum shown in Fig. 6 is due to band to band recombination, whereas the low energy peak corresponds to emission from tail states.

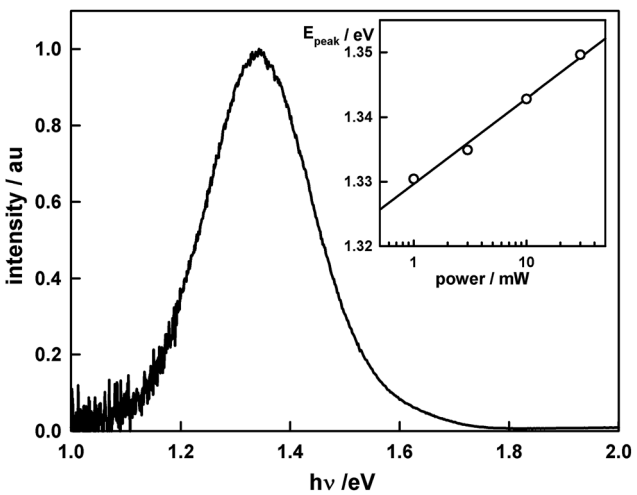

Fig. 5 Room temperature PL spectrum of CZTS platelet (laser intensity 10 mW). The inset shows the blue shift of the PL emission peak with increasing intensity.

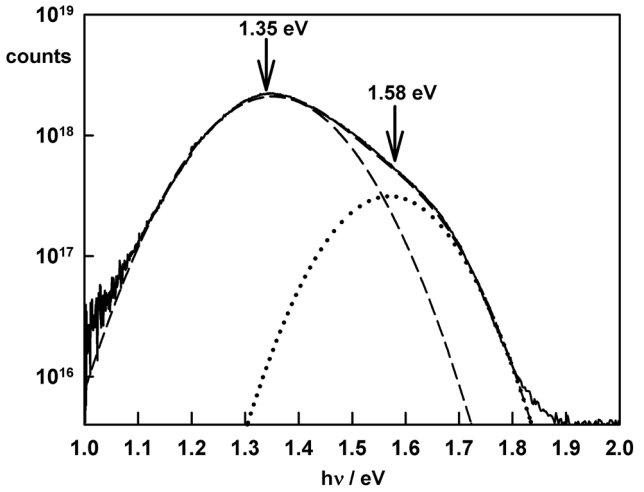

Fig. 6 PL spectrum of CZTS platelet showing shoulder at higher energy attributed to radiative band to band recombination (laser power 50 mW).

PL transients measured at room temperature for the platelet are illustrated in Fig. 7. The decay is slower when measured at 1.30 eV compared with 1.65 eV. The lifetimes obtained from the exponential fits shown in Fig. 7 are 3.5 ns (1.65 eV) and 6.8 ns (1.30 eV), similar to the 7.8 ns reported by Shin *et al.*[43] for an 8.4% efficient CZTS solar cell. However, the decay rates at the two photon energies are almost identical in the case of the needle ($\tau = 3.6$ ns: see ESI†).

The lifetimes derived here may not correspond to the lifetime of free electrons moving in CZTS since multiple trapping processes may be involved.[39,44–46] This makes it difficult to calculate electron diffusion lengths, since the electron mobility will be reduced from the free electron value by multiple trapping. Phoung *et al.*[45] have used time-resolved femtosecond transient reflectance and optical pump-probe terahertz spectroscopy to study free carrier dynamics in CZTS single crystals, and they attribute the relatively long (ns) electron lifetimes to thermal release of carriers from tail states.

Spectroscopic ellipsometry

Spectra of the real and imaginary components of the optical dielectric constant and the absorption coefficient obtained by fitting the ellipsometric data for the platelet sample are shown

Published on 12 December 2016. Downloaded by University of Milan - Bicocca on 09/01/2017 13:31:27.

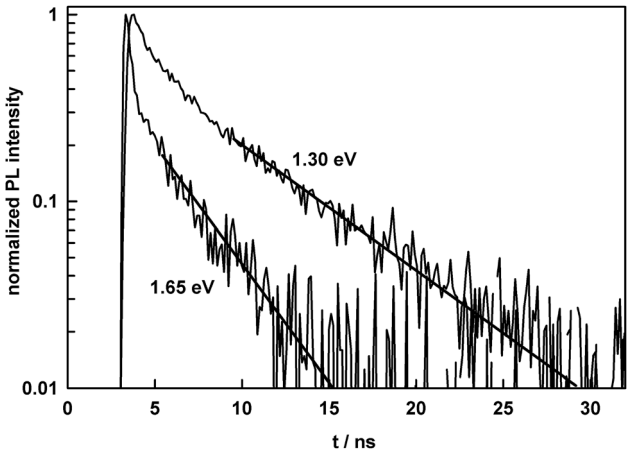

Fig. 7 Transient PL response of the CZTS platelet. Excitation energy 1.96 eV. Detection energies as shown.

in Fig. 8. Details of the fitting, as well as results for the needle sample, are given in the ESI,† which also includes a comparison with published optical data. The fitting used oscillators centred at 1.81, 2.60 and 4.27 eV. The absorption coefficient shows an exponential Urbach tail extending into the near infrared that is discussed below.

EQE measurements

Durant *et al.*[47] have reported electrolyte EQE measurements of natural kesterite crystals, but as far as we are aware, no detailed study of the photoresponse of synthetic CZTS crystals in contact with an electrolyte have been published previously. The EQE response of the single crystals was found to be strongly influenced by surface preparation. High EQE values could be obtained immediately after etching, but the photoresponse decayed slowly with time. The external quantum efficiency (EQE) for the semiconductor/electrolyte junction in the absence of surface recombination is given by the expression originally derived by Gärtner.[48]

$$\mathrm{EQE} = 1 - \frac{\exp(-\alpha W)}{1 + \alpha L_n} \quad (3)$$

Here W is the width of the space charge region, α is the wavelength dependent absorption coefficient and L_n is the diffusion length of electrons.

The EQE response of a freshly etched platelet crystal is shown in Fig. 9. Since the reflection loss is estimated to be of the order of 10% in the region where the EQE reaches a plateau, the spectrum indicates that essentially all photogenerated electrons are collected in the junction for photon energies above 1.7 eV. It follows that the second term on the right-hand side of the Gärtner equation must become negligible under these conditions. Near the band edge, we can assume that $\alpha L_n < 1$. In this case $-\ln(1 - \mathrm{EQE}_{corr}) = \alpha W$ (here EQE_{corr} is the EQE corrected for reflection losses).

Plots of $(\alpha h\nu)^2$ *vs.* $h\nu$ are commonly used to estimate the direct allowed bandgap (Tauc plots). The inset in Fig. 9 shows a plot of $[-h\nu \times \ln(1 - \mathrm{EQE}_{corr})]^2$ *vs.* photon energy, which is equivalent to the Tauc plot for a direct allowed transition. The intercept at 1.68 eV should therefore correspond to the optical bandgap, E_g, of the CZTS. A similar plot for the needle crystal gave a slightly lower bandgap of 1.64 eV (see ESI†). Tauc plots of the optical SE data for the platelet gave a slightly lower bandgap of 1.61 eV (see ESI†).

The exponential tail evident in the SE, EQE and Tauc plots is consistent with the existence of an Urbach tail associated with disorder in the CZTS crystal. The difficulties encountered when using Tauc plots for systems with sub-bandgap absorption (tail states) have been highlighted for the case of kesterites by Siebentritt *et al.*,[49] and these bandgap values should be considered approximate. As shown in the ESI,† the EQE response in the sub-bandgap energy range 1.4–1.7 eV can be fitted to an exponential Urbach distribution with $E_U = 2.2k_BT$, which is

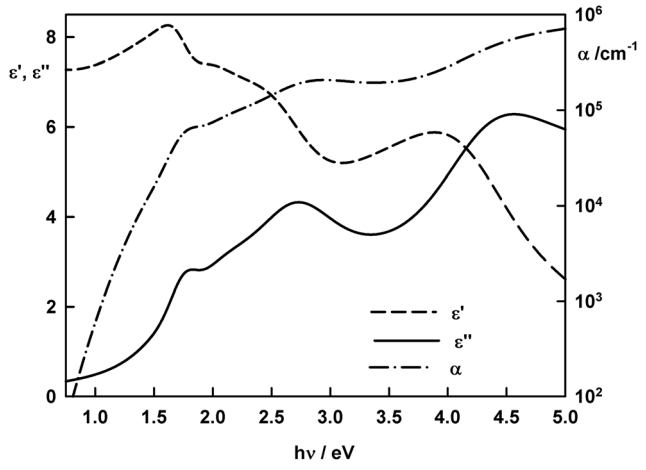

Fig. 8 Real and imaginary components of the optical dielectric constant for the CZTS platelet measured by spectroscopic ellipsometry. The figure also shows the absorption coefficient derived from the measurement.

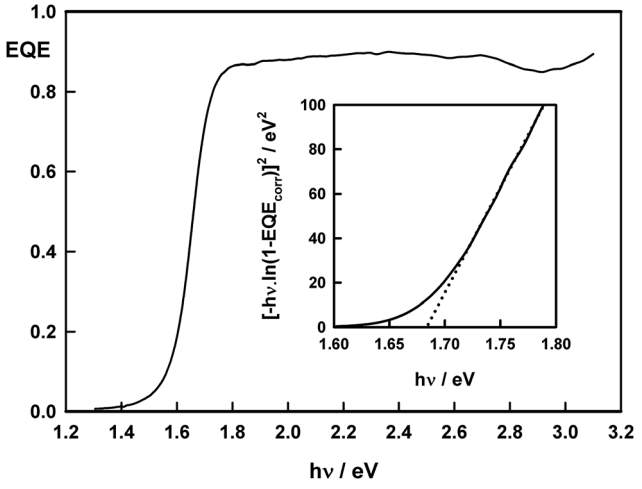

Fig. 9 EQE spectrum of CZTS platelet (uncorrected for reflection losses). Electrolyte; 0.1 M acetate buffer pH 4.5. Potential −1.0 V *vs.* Ag/AgCl. The insert shows a Tauc plot for a direct allowed transition ($E_g = 1.68$ eV).

 This journal is © The Royal Society of Chemistry 2016

Published on 12 December 2016. Downloaded by University of Milan - Bicocca on 09/01/2017 13:31:27.

considerably lower than the E_U value ($6.7k_BT$) derived from the SE data for the same energy range (see ESI†). The difference in Urbach energies suggests that lower energy optical transitions in the tail region lead to bound electron–hole states that require thermal activation to produce current in the external circuit and therefore have a lower chance of separation before recombination occurs.

If the semiconductor/electrolyte junction behaved ideally, the width of the space charge region should be controlled by the applied electrode potential, U, obeying the relationship $W \propto (U_{fb} - U)^{1/2}$, where U_{fb} is the flat band potential. Unfortunately, in the present case, attempts to measure the space charge capacitance as a function of applied potential by impedance spectroscopy revealed that the junction is not ideal due to the presence of a high surface state capacitance (see ESI†). This precluded full analysis of the potential dependence of the EQE spectra based on eqn (3), which can in principle give the absorption coefficient and the electron diffusion length, as demonstrated for p-GaP for example.[50] Nevertheless, the 'square' shape of the EQE spectrum in Fig. 9 shows that collection of minority carriers is very efficient even when the penetration depth of the light is large near the band edge. By contrast, the EQE spectra reported for high-performance CZTS solar cells generally show a slower rise from 1.4 eV to a peak at around 2.3 eV – see, for example, the EQE spectrum for a 2 μm CZTS absorber layer in a recent paper by Ren *et al.*[51]

Fig. 10 compares the measured EQE corrected for reflection losses with EQE plots calculated from the Gärtner equation (eqn (3)) for different values of the collection depth $W + L_n$ using values of the absorption coefficient derived from the SE measurements (*cf.* Fig. 8). Since reported doping densities for CZTS are of the order of 10^{16} cm^{-3}, the width of the space charge region under the conditions employed for EQE measurements has been taken as 300 nm (see ESI†). Using this value, the effect on the EQE spectrum of increasing the electron diffusion length was explored, and representative results are shown in Fig. 10. The fitting above *ca.* 1.75 eV indicates that the collection depth for minority carriers approaches 1 μm. This rather high value could indicate that the doping density is lower than assumed in the calculation. In the limit that $L_n \ll W$, W would be 1 μm, and the doping density would have to be *ca.* 10^{15} cm^{-3} to fit the spectrum.

It is apparent that the experimental EQE spectrum shows a much steeper onset than the spectra calculated using the α values obtained by SE. This can be explained if it is assumed that absorption of light in tails states below the band edge leads to bound states for which thermal excitation to create free charge carriers must compete with recombination.

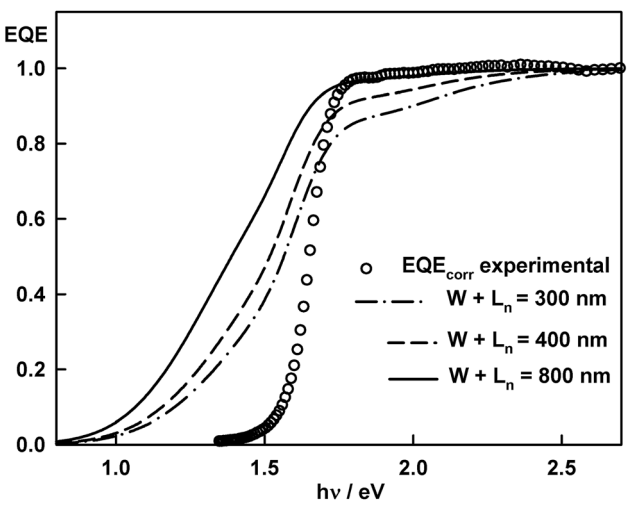

Fig. 10 Comparison of experimental EQE (Fig. 9, corrected for reflection losses) with EQE calculated using eqn (3) for the collection depth values shown. W was taken as 300 nm for the calculations, and L_n was varied. The α values were derived by spectroscopic ellipsometry.

Electrolyte electroreflectance

Electrolyte electroreflectance (EER) is a powerful technique for obtaining the bandgap of semiconductors. The method involves perturbing the electrical field in the space charge region by ac voltage modulation and detecting the synchronous changes in reflectance. Under low field conditions, the EER spectrum corresponds to the third derivative of the imaginary component of the optical dielectric constant,[52] and the results can be compared with those obtained by spectroscopic ellipsometry.[53] EER spectra can be modelled using a broadening parameter Γ that can be related to disorder and non-stoichiometry.[54,55] EER should therefore be a useful technique for characterizing cation disorder in CZTS. Fig. 11 shows the EER spectrum of the platelet crystal. A very similar EER spectrum was obtained for the needle (see ESI†).

Successful fitting of the EER spectrum required the use of two generalized line shape functions of the form proposed by Aspnes.[52,56]

$$\frac{\Delta R}{R} = \mathrm{Re}\left[Ce^{i\theta}\left(E - E_g - i\Gamma\right)^n\right] \quad (4)$$

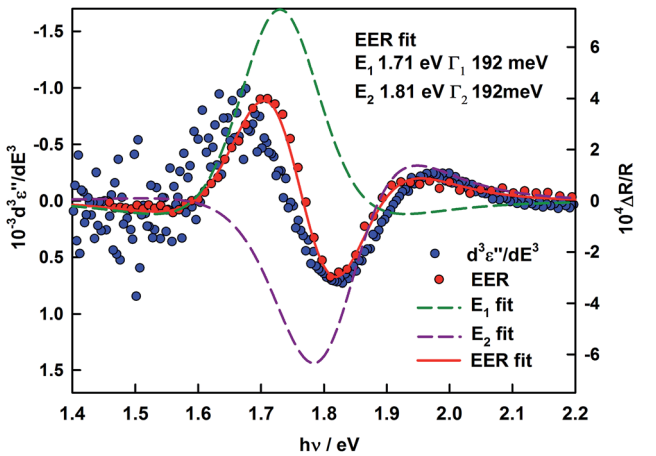

Fig. 11 EER spectrum of CZTS platelet showing fit to two transitions. The plot also shows the third derivative of the ε'' spectrum obtain by spectroscopic ellipsometry.

Published on 12 December 2016. Downloaded by University of Milan - Bicocca on 09/01/2017 13:31:27.

with $n = 5/2$ (3D critical point). Here $\Delta R/R$ is the normalized modulated reflectance, C is a scaling factor, θ is the phase projection factor, E is the photon energy, E_g is the bandgap energy and Γ is the broadening parameter. The EER response was found to depend linearly on the modulation amplitude, indicating that the low field expression is applicable[52] (see ESI†).

The fit shown in Fig. 11 corresponds to a superposition of two transitions at 1.71 eV and 1.81 eV, both values being higher than the bandgap, of *ca.* 1.68 eV derived from the Tauc plot in Fig. 9. The high Γ values obtained by the fitting of the EER spectra for CZTS provide further evidence of disorder leading to band energy fluctuations that effectively broaden the optical transitions (typical Γ values for single crystal binary semiconductors are considerably smaller, for example 53 meV for CdTe[57]). To check whether the EER spectrum does indeed correspond to the third derivative of ε'' as predicted by the Aspnes analysis, the SE data for the platelet crystal were differentiated, giving the result included in Fig. 11. The agreement confirms that the low field approximation is indeed valid.

The well-resolved EER spectrum shown in Fig. 11 differs significantly from spectra in the literature. Levcenco *et al.*[58] have reported room temperature EER spectra for CZTS single crystals grown by ICl_3 vapor transport, and their spectra (only shown over the range 1.2 to 1.6 eV) show a single peak at around 1.45 eV with very little response at higher energies. These authors also used the generalized line shape to analyse their EER spectra and reported A and B transitions at 1.457 eV and 1.464 eV. However, the line shapes of our EER spectra resemble more the EER spectra reported for CZTSe solar cells by Krämmer *et al.*[59] and by Krustok *et al.*[60] Clearly more work is needed to understand why our EER spectra differ so much from those reported in ref. 58.

Conclusions

Single crystals of CZTS have been grown with near-equilibrium disorder, as shown by near-resonance Raman spectroscopy. The band tail seen in the optical properties is attributed to residual disorder, which is also responsible for the red shift of the room temperature photoluminescence peak relative to the bandgap. The EQE spectra show much less evidence of the band tail, and this is attributed to a lower electron–hole separation efficiency for bound states created by sub-bandgap absorption. The bandgaps derived from Tauc plots of the optical and EQE data are in the range 1.60–1.64 eV, whereas the fitting of EER spectra indicates two adjacent transitions at higher energies (1.71 and 1.81 eV). This highlights the difficulty of using Tauc plots to determine the band gap in materials that have a high density of tail states.

The 100 meV separation of the transitions seen in the EER spectra could arise from crystal field splitting of the valence band, although it is higher than the 40 meV calculated by Persson *et al.*[17] for 0 K. The high value of the EQE in the plateau region of the EQE spectrum indicates 100% collection efficiency of photogenerated electron–hole pairs, while the shape of the spectrum is consistent with a collection depth approaching 1 μm. The electron lifetimes measured by PL decay are in the range 3.5–6.8 ns.

The effect on the optoelectronic properties of including a sodium source in the starting materials for CZTS crystal growth appears to be minor. This may indicate that the beneficial influence of sodium on the performance of CZTS solar cells is more likely to be associated with grain boundary effects.

Acknowledgements

This work was supported by the EPSRC PVTeam project (Grant No. EP/L017792/1). BW and HJS acknowledge EPSRC grant EP/L024667/1. TMN is funded by EPSRC Doctoral Training Centre in Sustainable Chemical Technologies at the University of Bath (Grant No. EP/G03768X/1). JdW thanks FNR for funding from the EATSS project and FB thanks FNR for funding from the CURI-K project. The authors acknowledge useful discussions with Jonathan Scragg and Shuyi Li (Angstrom Institute Uppsala) as well as Leo Choubrac and Michaël Paris (Nantes). The authors thank Shuyu Li for providing CZTS thin film optical data for comparison.

References

1 S.-Y. Li, C. Hägglund, Y. Ren, J. J. S. Scragg, J. K. Larsen, C. Frisk, K. Rudisch, S. Englund and C. Platzer-Björkman, *Sol. Energy Mater. Sol. Cells*, 2016, **149**, 170–178.
2 K. Ito, *Copper Zinc Tin Sulfide-Based Thin Film Solar Cells*, Wiley, Chichester, United Kingdom, 2015.
3 S. Adachi, *Earth-Abundant Materials for Solar Cells. Cu_2-II-IV-VI_4 Semiconductors*, Wiley, Chichester, United Kingdom, 2015.
4 T. Todorov, O. Gunawan, S. J. Chey, T. G. de Monsabert, A. Prabhakar and D. B. Mitzi, *Thin Solid Films*, 2011, **519**, 7378–7381.
5 A. Walsh, S. Chen, S.-H. Wei and X.-G. Gong, *Adv. Energy Mater.*, 2012, **2**, 400–409.
6 S. Siebentritt, *Thin Solid Films*, 2013, **535**, 1–4.
7 W. Wang, M. T. Winkler, O. Gunawan, T. Gokmen, T. K. Todorov, Y. Zhu and D. B. Mitzi, *Adv. Energy Mater.*, 2014, **4**, 1301465.
8 J. J. S. Scragg, J. K. Larsen, M. Kumar, C. Persson, J. Sendler, S. Siebentritt and C. P. Bjorkman, *Phys. Status Solidi B*, 2016, **253**, 247–254.
9 J. J. S. Scragg, L. Choubrac, A. Lafond, T. Ericson and C. Platzer-Björkman, *Appl. Phys. Lett.*, 2014, **104**, 041911.
10 S. Bourdais, C. Choné, B. Delatouche, A. Jacob, G. Larramona, C. Moisan, A. Lafond, F. Donatini, G. Rey, S. Siebentritt, A. Walsh and G. Dennler, *Adv. Energy Mater.*, 2016, **6**, 1502276.
11 D. B. Mitzi, O. Gunawan, T. K. Todorov, K. Wang and S. Guha, *Sol. Energy Mater. Sol. Cells*, 2011, **95**, 1421–1436.
12 D. Colombara, S. Delsante, G. Borzone, J. M. Mitchels, K. C. Molloy, L. H. Thomas, B. G. Mendis, C. Y. Cummings, F. Marken and L. M. Peter, *J. Cryst. Growth*, 2013, **364**, 101–110.

 This journal is © The Royal Society of Chemistry 2016

Published on 12 December 2016. Downloaded by University of Milan - Bicocca on 09/01/2017 13:31:27.

13 L. E. Valle Rios, K. Neldner, G. Gurieva and S. Schorr, *J. Alloys Compd.*, 2016, **657**, 408–413.
14 T. K. Todorov, K. B. Reuter and D. B. Mitzi, *Adv. Mater.*, 2010, **22**, E156–E159.
15 D. Dumcenco and Y.-S. Huang, *Opt. Mater.*, 2013, **35**, 419–425.
16 P. A. Fernandes, P. M. P. Salome, A. F. da Cunha and B.-A. Schubert, *Thin Solid Films*, 2011, **519**, 7382–7385.
17 C. Persson, R. Chen, H. Zhao, M. Kumar and D. Huang, in *Copper Zinc Tin Sulfide-Based Thin Film Solar Cells*, ed. K. Ito, Wiley, Chichester, United Kingdom, 2015, ch. 4, p. 421.
18 L. J. Farrugia, *J. Appl. Crystallogr.*, 1999, **32**, 837–838.
19 G. Sheldrick, *XPREP. Space Group Determination and Reciprocal Space Plots*, 1991.
20 G. M. Sheldrick, *Release 97-2*, University of Göttingen, Germany, 1997.
21 G. M. Sheldrick, *Acta Crystallogr., Sect. A: Found. Crystallogr.*, 2008, **64**, 112–122.
22 A. Lafond, L. Choubrac, C. Guillot-Deudon, P. Fertey, M. Evain and S. Jobic, *Acta Crystallogr., Sect. B: Struct. Sci., Cryst. Eng. Mater.*, 2014, **70**, 390–394.
23 L. Choubrac, A. Lafond, C. Guillot-Deudon, Y. Moëlo and S. Jobic, *Inorg. Chem.*, 2012, **51**, 3346–3348.
24 A. Lafond, L. Choubrac, C. Guillot-Deudon, P. Deniard and S. Jobic, *Z. Anorg. Allg. Chem.*, 2012, **638**, 2571–2577.
25 L. Choubrac, M. Paris, A. Lafond, C. Guillot-Deudon, X. Rocquefelte and S. Jobic, *Phys. Chem. Chem. Phys.*, 2013, **15**, 10722–10725.
26 L. Choubrac, A. Lafond, M. Paris, C. Guillot-Deudon and S. Jobic, *Phys. Chem. Chem. Phys.*, 2015, **17**, 15088–15092.
27 H. Nozaki, T. Fukano, S. Ohta, Y. Seno, H. Katagiri and K. Jimbo, *J. Alloys Compd.*, 2012, **524**, 22–25.
28 S. Schorr, *Sol. Energy Mater. Sol. Cells*, 2011, **95**, 1482–1488.
29 T. Gurel, C. Sevik and T. Cagin, *Phys. Rev. B: Condens. Matter Mater. Phys.*, 2011, **84**, 205201.
30 A. Khare, B. Himmetoglu, M. Johnson, D. J. Norris, M. Cococcioni and E. S. Aydil, *J. Appl. Phys.*, 2012, **111**, 083707.
31 S. Chen, X. G. Gong, A. Walsh and S.-H. Wei, *Appl. Phys. Lett.*, 2009, **94**, 041903.
32 G. Rey, T. P. Weiss, J. Sendler, A. Finger, C. Spindler, F. Werner, M. Melchiorre, M. Hála, M. Guennou and S. Siebentritt, *Sol. Energy Mater. Sol. Cells*, 2016, **151**, 131–138.
33 K. Rudisch, Y. Ren, C. Platzer-Björkman and J. Scragg, *Appl. Phys. Lett.*, 2016, **108**, 231902.
34 A. Ritscher, M. Hoelzel and M. Lerch, *J. Solid State Chem.*, 2016, **238**, 68–73.
35 M. Paris, L. Choubrac, A. Lafond, C. Guillot-Deudon and S. Jobic, *Inorg. Chem.*, 2014, **53**, 8646–8653.
36 G. Rey, A. Redinger, J. Sendler, T. P. Weiss, M. Thevenin, M. Guennou, B. E. Adib and S. Siebentritt, *Appl. Phys. Lett.*, 2014, **105**, 112106.
37 G. H. Vineyard, *Phys. Rev.*, 1956, **102**, 981–992.
38 L. Van Puyvelde, J. Lauwaert, P. F. Smet, S. Khelifi, T. Ericson, J. J. Scragg, D. Poelman, R. Van Deun, C. Platzer-Björkman and H. Vrielinck, *Thin Solid Films*, 2015, **582**, 146–150.
39 L. Quang Phuong, M. Okano, Y. Yamada, A. Nagaoka, K. Yoshino and Y. Kanemitsu, *Appl. Phys. Lett.*, 2013, **103**, 191902.
40 J. P. Leitao, N. M. Santos, P. A. Fernandes, P. M. P. Salome, A. F. da Cunha, J. C. Gonzalez, G. M. Ribeiro and F. M. Matinaga, *Phys. Rev. B: Condens. Matter Mater. Phys.*, 2011, **84**, 024120.
41 T. Schmidt, K. Lischka and W. Zulehner, *Phys. Rev. B: Condens. Matter Mater. Phys.*, 1992, **45**, 8989–8994.
42 T. Gershon, B. Shin, N. Bojarczuk, T. Gokmen, S. Lu and S. Guha, *J. Appl. Phys.*, 2013, **114**, 154905.
43 B. Shin, O. Gunawan, Y. Zhu, N. A. Bojarczuk, S. J. Chey and S. Guha, *Progress in Photovoltaics: Research and Applications*, 2013, **21**, 72–76.
44 M. Okano, L. Q. Phuong and Y. Kanemitsu, *Phys. Status Solidi B*, 2015, **252**, 1219–1224.
45 L. Q. Phuong, M. Okano, Y. Yamada, G. Yamashita, T. Morimoto, M. Nagai, M. Ashida, A. Nagaoka, K. Yoshino and Y. Kanemitsu, *Appl. Phys. Lett.*, 2014, **105**, 231902.
46 M. Maiberg, T. Hölscher, S. Zahedi-Azad, W. Fränzel and R. Scheer, *Appl. Phys. Lett.*, 2015, **107**, 122104.
47 B. K. Durant and B. A. Parkinson, *Sol. Energy Mater. Sol. Cells*, 2016, **144**, 586–591.
48 W. W. Gärtner, *Phys. Rev.*, 1959, **116**, 84–87.
49 S. Siebentritt, G. Rey, A. Finger, D. Regesch, J. Sendler, T. P. Weiss and T. Bertram, *Sol. Energy Mater. Sol. Cells*, 2016, **158**(2), 126–129.
50 R. Peat and L. M. Peter, *Appl. Phys. Lett.*, 1987, **51**, 328–330.
51 Y. Ren, J. J. S. Scragg, C. Frisk, J. K. Larsen, S.-Y. Li and C. Platzer-Björkman, *Phys. Status Solidi A*, 2015, **212**, 2889–2896.
52 D. E. Aspnes, *Surf. Sci.*, 1973, **37**, 418–442.
53 P. M. Raccah, J. W. Garland, Z. Zhang, U. Lee, D. Z. Xue, L. L. Abels, S. Ugur and W. Wilinsky, *Phys. Rev. Lett.*, 1984, **53**, 1958–1961.
54 L. E. A. Berlouis, L. M. Peter, M. G. Astles, J. Gough, R. G. Humphreys, S. J. C. Irvine and V. Steward, *J. Appl. Phys.*, 1987, **62**, 4518–4522.
55 P. M. Raccah, U. Lee, S. Ugur, D. Z. Xue, L. L. Abels and J. W. Garland, *J. Vac. Sci. Technol., A*, 1985, **3**, 138–142.
56 D. E. Aspnes, in *Handbook on Semiconductors. Vol. 2. Optical Properties Solids*, ed. T. S. Moss and M. Balkanski, North-Holland, 1972, vol. 2, pp. 109–154.
57 W. S. Enloe, J. C. Parker, J. Vespoli, T. H. Myers, R. L. Harper and J. F. Schetzina, *J. Appl. Phys.*, 1987, **61**, 2005–2010.
58 S. Levcenco, D. Dumcenco, Y. P. Wang, Y. S. Huang, C. H. Ho, E. Arushanov, V. Tezlevan and K. K. Tiong, *Opt. Mater.*, 2012, **34**, 1362–1365.
59 C. Krämmer, C. Huber, C. Zimmermann, M. Lang, T. Schnabel, T. Abzieher, E. Ahlswede, H. Kalt and M. Hetterich, *Appl. Phys. Lett.*, 2014, **105**, 262104.
60 J. Krustok, T. Raadik, M. Grossberg, S. Giraldo, M. Neuschitzer, S. López-Marino and E. Saucedo, *Mater. Sci. Semicond. Process.*, 2015, **39**, 251–254.